Evaluation of longitudinal time-lapsed *in vivo* micro-CT for monitoring fracture healing in mouse femur defect models

Esther Wehrle[1], Duncan C Tourolle né Betts[1], Gisela A Kuhn[1], Ariane C Scheuren[1], Sandra Hofmann[1,2], Ralph Müller[1*]

[1] Institute for Biomechanics, ETH Zurich, Zurich, Switzerland, [2] Department of Biomedical Engineering and Institute for Complex Molecular Systems, Eindhoven University of Technology, The Netherlands.

Corresponding author:

Ralph Müller, PhD

Institute for Biomechanics

ETH Zurich

Leopold-Ruzicka-Weg 4

8093 Zurich, Switzerland

Email: ram@ethz.ch

Abstract

Longitudinal *in vivo* micro-computed tomography (micro-CT) is of interest to non-invasively capture the healing process of individual animals in preclinical fracture healing studies. However, it is not known whether longitudinal imaging itself has an impact on callus formation and remodeling. In this study, a scan group received weekly micro-CT measurements (week 0-6), whereas controls were only scanned post-operatively and at week 5 and 6. Registration of consecutive scans using a branching scheme (bridged vs. unbridged defect) combined with a two-threshold approach enabled assessment of localized bone turnover and mineralization kinetics relevant for monitoring callus remodeling. Weekly micro-CT application did not significantly change any of the assessed callus parameters in the defect and periosteal volumes. This was supported by histomorphometry showing only small amounts of cartilage residuals in both groups, indicating progression towards the end of the healing period. Also, immunohistochemical staining of Sclerostin, previously associated with mediating adverse radiation effects on bone, did not reveal differences between groups.

The established longitudinal *in vivo* micro-CT-based approach allows monitoring of healing phases in mouse femur defect models without significant effects of anesthesia, handling and radiation on callus properties. Therefore, this study supports application of longitudinal *in vivo* micro-CT for healing-phase-specific monitoring of fracture repair in mice.

42 **Introduction**

43 Adequate monitoring and characterization of the healing process is important in preclinical
44 fracture healing studies. One recent approach to non-invasively capture the formation and
45 remodeling of the osseous fracture callus is the repeated application of *in vivo* micro-
46 computed tomography (micro-CT)[1-3], allowing for three-dimensional assessment of callus
47 structures over time. A further development is the consecutive registration of time-lapsed *in*
48 *vivo* callus measurements[4]. In a recent study, we developed a method for registration of
49 time-lapsed *in vivo* scans in a femur defect model in mice using a branching scheme
50 (registration of whole scan for bridged defects; separate registration of the two fragments
51 for unbridged defects)[5], so that we are now able to also assess dynamic parameters such as
52 bone formation and resorption. In combination with two- and multi-threshold approaches
53 applied in recent studies[5,6], this allows for better understanding of localized bone turnover
54 and mineralization kinetics during callus formation and remodeling. Whereas many studies
55 focused on understanding the early healing phases (inflammation, repair) with the aim of
56 increasing bone formation and achieving earlier bone union, recent studies also indicate a
57 potential to improve fracture healing outcome via modulation of callus remodeling[7-9]. To
58 address this, time-lapsed *in vivo* micro-CT-based monitoring approaches seem particularly
59 suitable, as not only bone formation but also bone resorption can be reliably monitored over
60 time. Furthermore, as each animal can be followed individually throughout the healing
61 process with low variance in the assessed parameters, animal numbers can be reduced
62 compared to well-established cross-sectional studies with endpoint three-dimensional
63 micro-CT and two-dimensional histological callus evaluation.

In non-fractured bone, longitudinal time-lapsed *in vivo* micro-CT has been increasingly used to monitor changes in bone properties associated with different diseases and external factors, e.g. estrogen-deficiency[10-12], mechanical-(un)loading[13-15], and drug application[16]. However, several studies indicate that anesthesia, cumulative radiation dosage and stress due to the required handling for the CT measurements may have effects on animal well-being and on trabecular and cortical bone properties[11,17-21]. Isoflurane is the most commonly used inhalation anesthetic in rodents[22], characterized by a quick on- and offset of anesthesia and low metabolism rate[22]. According to the EU Directive 2010/63, the severity of repeated isoflurane anesthesia can be categorized as mild, although repeated anesthesia was considered worse than a single session with sex-dependent differences in perceiving the severity of a procedure[17]. Specifically, female mice were shown to be more susceptible to anesthesia-induced effects on well-being compared to male mice[17]. Nevertheless, in both sexes repeated isoflurane anesthesia caused only short-term mild distress and impairment of well-being, mainly in the immediate post-anesthetic period[17]. Radiation has also been shown to have dosage-dependent effects on bone cells *in vivo* and *in vitro*: Whereas high dose x-ray radiation (2.5-8Gy) was associated with reduced osteoblast and osteoclast proliferation[23-25], lower doses (<2Gy) had a stimulatory effect on osteoclasts. Some studies reported radiation-associated effects on structural bone parameters with stronger and earlier effects seen in trabecular bone compared to cortical bone, whereas other studies did not see any changes[11,19,21,26,27]. Similarly, pre- and post-operative radiation treatments have been associated with changes in fracture healing. Whereas high dose x-ray radiation (5-8Gy) was associated with an impairment of fracture healing, lower doses (0.5-1Gy) accelerated endochondral and intramembranous ossification during the repair process[28-31]. These

87 findings indicate the importance of study-specific adaptation of micro-CT protocols, and to
88 protect animals scanning times and radiation settings should be minimized.

89 Recently, several fracture healing studies have applied longitudinal *in vivo* micro-CT to
90 monitor callus formation under different conditions (e.g. osteoporosis, polytrauma) and
91 treatments (e.g. mechanical loading, pharmaceuticals)[2-4,32,33]. However, none of these
92 studies assessed, whether longitudinal imaging itself has an impact on callus formation and
93 remodeling. As several studies have reported adverse effects of longitudinal imaging during
94 normal bone remodeling (e.g. reduction in trabecular and cortical thickness)[11,19,21,27], there is
95 a need to also assess imaging-associated impact on the callus formation during the highly
96 metabolically active process of fracture healing.

97 Therefore, the objectives of this study were to establish an *in vivo* micro-CT based approach
98 for longitudinal monitoring of fracture healing in a mouse femur defect model and to assess
99 the combined effect of radiation, anesthesia and handling associated with weekly time-
100 lapsed micro-CT measurements on callus properties during the remodeling phase of fracture
101 healing.

102

103 **Results**

104 In order to enable longitudinal monitoring of fracture healing in single animals, we
105 established a time-lapsed *in vivo* micro-CT based approach for mouse femur defect models.
106 By registration of consecutive scans, structural and dynamic callus parameters can be
107 followed in three callus sub-volumes (defect center, defect periphery, cortical fragment
108 periphery) and the adjacent cortical fragments over time (Figure 1). To capture potential

effects of consecutive micro-CT measurements on callus properties, bone parameters of a scan group subjected to weekly measurements between weeks 0 and 6 were compared to control animals, that were scanned only post-operatively (d0) and after 5 and 6 weeks, respectively (for detailed study design see Supplementary Fig. S1 online).

General physical observation

All mice recovered rapidly from surgery. During the healing period, in both groups, the animals' body weight did not significantly change compared to pre-operative values without significant differences between the two groups (see Supplementary Fig. S1 online). We also assessed the social interaction between mice (animals sitting in groups vs. separated from others) and the nesting behavior (start of nest building after surgery). Specifically, all animals started to build nests on the day of surgery and were found in groups in the nest in the morning of post-operative day 1. Throughout the further healing period social interaction between mice and nesting behavior did not differ from pre-surgical observations and was similar for animals of the scan and control groups.

Volumes of interest (VOI) for evaluation by time-lapsed *in vivo* micro-CT

In order to exclude bias in the further micro-CT analyses, we compared the size of the different VOIs (depicted in Fig. 1) in the control and the scan group. One animal from the scan group could not be included in the analysis due to failure in VOI generation caused by too little cortical bone being present in the field of view (for details on VOI generation see [5]). The VOIs encompassed the following volume for the control (n=8) and scan group (n=10): 2.51±0.34mm^3 vs. 2.60±0.34mm^3 for the defect center (DC), 17.26±2.21mm^3 vs.

132 18.73±4.64mm^3 for the defect periphery (DP), 1.86±0.48mm^3 vs. 1.73±0.45mm^3 for the
133 cortical fragments (FC), 14.47±3.30mm^3 vs. 13.10±2.66mm^3 for the fragment periphery (FP).
134 The total volume (TOT=DC+DP+FC+FP) between the inner pins of the fixator was
135 36.10±2.81mm^3 for the control and 36.15±3.74mm^3 for the scan group. No significant
136 differences in volume were detected in any of the VOIs between groups.
137
138 **Longitudinal monitoring of fracture healing by time-lapsed *in vivo* micro-CT**
139 In the scan group (n=10), the repeated micro-CT scans (1x/week, Fig. 2) covered the period
140 from the day of the defect surgery (d0) until post-operative week 6 with distinct callus
141 characteristics indicative of the different healing phases (inflammation, repair, remodeling;
142 significant weekly differences in bone parameters indicated in Fig. 3). From week 0-1 to
143 week 1-2 a significant 5.7x increase in bone formation was detected (Fig. 3a) in the total VOI
144 (TOT=DC+DF+FC+FP, p<0.0001; Fig. 1), indicating progression from the inflammation to the
145 reparative phase. This led to a significant gain in bone volume by week 2 (BV/TV_{week2}: 39±7%
146 vs. BV/TV_{week0}: 25±3%, p=0.0134; Fig. 3b). From week 1-2 to week 2-3 a significant 2.8x
147 increase in resorptive activities (p=0.0020; Fig. 3a) was seen, indicating the progression from
148 the repair to the remodeling phase. Two weeks after surgery the highly mineralized bone
149 fraction in the TOT VOI was significantly lower compared to the post-operative
150 measurement (BV_{645}/BV_{395} in week 2: 59±5% vs. BV_{645}/BV_{395} in week 0: 84±1%, p<0.0001),
151 indicating formation of mineralized callus of low density. From post-operative week 2
152 onwards, the highly mineralized bone fraction in the TOT VOI gradually increased in all
153 subsequent weeks of the healing period reaching statistical significance by week 5
154 (BV_{645}/BV_{395} in week 2: 59±5% vs. BV_{645}/BV_{395} in week 5: 79±3%, p=0.0134; Fig. 3c).

155

156 In order to better capture the regions where bone is mainly formed and resorbed, we
157 evaluated the different VOIs separately (Table 1): In the early post-operative phase from
158 week 0-1 to week 1-2 a strong onset of bone formation was seen in the DC and FP sub-
159 volumes, leading to significant 11.8x and 3.4x gain in mineralized tissue from week 0 to week
160 2 for DC (p=0.0090) and FP (p=0.0091), respectively. This indicates that both intra-cortical as
161 well as periosteal callus formation takes place in this femur defect model. In both VOIs bone
162 formation triggered the initiation of bone resorption from week 2-3. In detail, there was a
163 significant 6.2x and 2.9x increase in bone resorption from week 1-2 to week 2-3 in the DC
164 (p=0.0040) and the FP VOI (p=0.0079), respectively. Compared to the DC and FP VOIs, the
165 initiation of bone formation was much less pronounced in the DP sub-volume with less
166 deposition of mineralized tissue leading to only little peripheral callus formation in this VOI
167 (week 2-6) and subsequently low bone resorption activities from week 2-3 to week 5-6. In all
168 three regions (DC, DP, FP) the fraction of highly mineralized bone considerably increased
169 from week 2 to week 5 (+192%, +774%, +227%), indicating callus maturation. In this femur
170 defect model, callus formation and remodeling mainly took place in the defect region (DC)
171 with only little peripheral callus formation and remodeling (DP). Looking at the cortical
172 fragments (FC), a significant 3.2x increase in resorptive activities was detected in week 1-2
173 compared to week 0-1 (p=0.0421), whereas no significant weekly change in bone formation
174 activities was seen in this region throughout the assessed healing period. This resulted in a
175 significant 24% reduction in bone volume from week 0 to week 4 (p=0.0091). The fraction of
176 highly mineralized bone also gradually decreased in the remaining osseous tissue reaching

statistical significance by week 3 (BV_{645}/BV_{395} in week 3 reduced by 9% compared to week 0, p=0.0027).

Influence of the longitudinal *in vivo* micro-CT protocol on callus properties

To assess the combined effects of radiation, anesthesia and handling associated with weekly micro-CT measurements (week 0 - week 6) on callus properties, callus parameters of the scan group were compared to control animals that were scanned only directly post-operatively (d0) and after 5 and 6 weeks (Fig. 4). To exclude bias in the further micro-CT analyses, we assessed the post-operative bone volume (BV/TV on d0) and did not see any significant differences between groups: 1.82±0.39% (control) vs. 1.47±0.15% (scan) in DC, 0.16±0.12% (control) vs. 0.13±0.06% (scan) in DP, 56.82±2.31% (control) vs. 57.14±6.99% (scan) in FC, 4.66±0.30% (control) vs. 4.74±0.76% (scan) in FP, 26.92±4.69% (control) and 24.90±2.88% (scan) in TOT.

During the remodeling phase (post-operative weeks 5-6), no significant difference in bone turnover was seen in the total volume (TOT) between the inner pins of the fixator (BFR: 0.76±0.23% in controls, 0.64±0.15% in scan group; BRR: 0.82±0.25% in controls, 0.78±0.26% in scan group). Also, bone volume did not significantly change due to the applied micro-CT protocol with a similar fraction of highly mineralized bone after 5 weeks (BV_{645}/BV_{395}: 79±3% in controls, 79±3% in scan group) and 6 weeks (BV_{645}/BV_{395}: 81±3% in controls, 82±4% in scan group).

199 As radiation effects are known to vary for different bone cell types and locations[30,34,35], we
200 assessed the four sub-volumes separately (Table 2). The applied micro-CT protocol did not
201 significantly affect bone formation and resorption activities in the callus VOIs (DC, DP and FP)
202 from week 5-6 with similar bone volume observed in week 5 and 6 for controls and scanned
203 animals. In both groups, bone volume remained stable from week 5 to week 6, whereas the
204 density of the mineralized tissue increased during the same period (DC, DP, FP). Looking at
205 the adjacent cortical fragments (FC) also no significant differences were detected in any of
206 the assessed parameters between the control group and the scan group. Similarly to the
207 callus VOIs, bone volume also remained stable in this region from week 5 to week 6.
208 However, in contrast to the callus VOIs, the density of the mineralized tissue in the cortical
209 VOI FC did not change from week 5 to week 6. In week 6, the FC VOI comprised 33% and
210 35% of the osseous tissue in the total VOI (TOT) for the control and scan group, respectively.
211 In the DC VOI, 37% (control group) and 36% (scan group) of the total bone volume were
212 seen. Less osseous tissue was detected in the two peripheral VOIs, 11% (control group) and
213 12% (scan group) in the DP and 19% (control group) and 17% (scan group) in the FP VOI.
214
215 As group comparisons were only performed from week 5-6, we particularly focused on the
216 defect VOIs (DC+DP) which are most important for evaluating later healing time points
217 during the remodeling phase of fracture healing. No significant differences in bone turnover,
218 bone volume and mineralization were seen between the scan and control group (Figure 4 d-
219 f, Table 2). In addition, according to the standard clinical evaluation of X-rays, the number of
220 bridged cortices per callus was evaluated in two perpendicular planes and animals with ≥3
221 bridged cortices were categorized as healed. By week 5, cortical bridging occurred in 75% of

222 the control animals and 64% of the scanned animals (Table 3). However, we noticed that
223 non-unions only occurred in defects of ≥1.5mm length. Although the mean defect length
224 (1.45mm±0.16 in controls, 1.47mm±0.16 in scan group) did not significantly differ between
225 groups (p=0.816), the percentage of animals with defects ≥1.5mm was different in the
226 control and the scan group (55% vs. 38%; Table 3). Taking into account only these defects
227 (≥1.5mm length), both groups had a non-union rate of 67% indicating no significant effect of
228 the chosen micro-CT protocol on clinical fracture healing outcome.
229
230 **Histology**
231 Histomorphometric analysis of Safranin-O stained sections did not show any significant
232 differences in tissue composition (bone, cartilage, fibrous tissue, bone marrow) in the former
233 defect region between the control and the scan group six weeks after osteotomy (Fig. 5,
234 Supplementary Fig. S2 online). The bone tissue fraction was 38+7% and 32+6% for the
235 control and the scan group, respectively. Hardly any cartilage residuals (< 1% of total area)
236 were present in both groups indicating progression of the healing process in the final
237 remodeling stage (Supplementary Fig. S3 online).
238
239 As radiation-mediated decreased bone formation by osteoblasts has previously been
240 associated with the inhibition of osteoanabolic Wnt-signaling[36], we assessed Sclerostin
241 expression in the defect region by immunohistochemistry. Visual inspection did not reveal
242 any differences in staining intensity and amount of Sclerostin between the scan and control
243 group (Fig. 5).
244

245 **Discussion**

246 In this study, longitudinal *in vivo* micro-CT was applied for monitoring the process of fracture
247 healing in mice. In addition, the combined effect of radiation, anesthesia and handling
248 associated with the established imaging approach on callus parameters was assessed. Until
249 now, preclinical fracture healing studies predominantly have a cross-sectional study design
250 with end-point callus evaluation in sub-groups of animals at different time points during the
251 healing period. Only recently, several studies in murine diaphyseal femur defect models
252 stabilized by external fixation[2-4,32] or intramedullary nails[33], have applied longitudinal *in vivo*
253 micro-CT to monitor the healing progression in each animal over time. These studies were
254 able to consecutively assess callus parameters (e.g. callus volume and density) at specific
255 time points during the healing process for up to 12 weeks[2-4,32,33]. By registering consecutive
256 scans, we were now able to also include dynamic parameters such as bone formation and
257 resorption in our micro-CT based monitoring approach for fracture healing (for details on
258 method see [5]). This allows for characterization of the different healing phases seen by
259 changes in formation and resorption in the osseous callus volume. Compared to histology-
260 based determination of the bone formation rate via *in vivo* application of fluorescent dyes
261 (e.g. calcein, alizarin), our micro-CT-based analysis with registration of consecutive scans also
262 allowed for assessment of the bone resorption rate in individual animals. Furthermore,
263 implementation of a two-threshold approach allowed to monitor mineralization kinetics of
264 the fracture callus. Our micro-CT-based approach is therefore particularly suited to better
265 understand callus remodeling under different conditions (e.g. premedication with
266 bisphosponates and associated inhibition of callus remodeling) and to assess
267 pharmacological and mechanical therapies targeting callus remodeling.

268 Specifically, we saw that the initiation of bone formation (maximum in week 2-3), indicating
269 the onset of the reparative phase, triggered bone resorption (maximum in week 3-4) with
270 maximum osseous callus volumes in week 3. These observations are in line with cross-
271 sectional histomorphometric analyses in similar defect models, where maximum callus area
272 was seen in weeks 2 and 3[37-39]. From week 4 to week 6, bone formation and resorption
273 continuously decreased to levels (BFR ≤ 1%/day; BRR ≤ 0.8%/day) seen in normal bone
274 remodeling of trabecular and cortical bone in mice[14,40-43], indicating proceeding towards the
275 end of the healing process. Whereas these remodeling activities also led to a decrease in
276 callus volume from week 4 to week 6, the fraction of highly mineralized bone increased
277 during the same period indicating advanced callus maturation. These observations were
278 further supported by histology with no remaining cartilage in the defect region of unions and
279 only a small amount of cartilage residuals in some non-unions. The findings are also in
280 accordance with previous longitudinal studies of up to 4 weeks in mice[2,3,32] and 8 weeks in
281 rats[4] mainly focusing on the inflammation and reparative phase. Similar to our study, the
282 bone volume continuously increased during the 4/8 week healing period, although no
283 remodeling to the original bone geometry was seen due to the shorter observation period.
284 One study in ovariectomized rats with a 12-week post-operative monitoring period detected
285 maximum osseous callus volumes by week 6, which diminished thereafter, whereas bone
286 mineral density continuously increased until week 12, similar to our findings. This indicates
287 that during the reparative phase first low-density bone is formed, which is then further
288 mineralized during the remodeling phase of fracture healing. Looking at the functional
289 fracture healing outcome, complete cortical bridging was seen in 64% of the animals, which
290 is similar to other studies (60-62%) using similar femur defect models with relatively stiff

291 external fixation (fixator stiffness measured in our study 24N/mm) in mice[2,44]. These
292 commercially available rigid external fixators are widely used in fracture healing studies as
293 they also allow for the assessment of biomaterials in non-union defects (induced by
294 increasing the defect size). Borgiani et al.[37] have recently extensively characterized the
295 healing process (week 1-3) using external fixators of similar stiffness and observed
296 endochondral ossification processes, albeit less pronounced compared to semi-rigid fixation.
297 When comparing the outcome of these studies using rigid fixation, it is important to consider
298 differences in defect sizes: 0.7mm^2, 1.19±0.25 mm[44], 1.47±0.16mm (this study). In contrast
299 to the other studies, we saw the manifestation of non-unions only in defects ≥1.5mm. This
300 might be partially due to the fact that in some studies the exact defect length might have
301 differed from the reported value (saw diameter used for osteotomy) and that non-union
302 formation was assessed irrespective of defect length. Overall, all longitudinal fracture
303 healing studies using *in vivo* micro-CT were able to follow the healing progression in single
304 animals, thereby reducing variance of outcome parameters compared to cross-sectional
305 studies, also allowing for reduction of animals per group considering the 3R principles of
306 animal welfare[45,46]. However, when applying longitudinal *in vivo* micro-CT, the effect of
307 repeated anesthesia, handling and radiation associated with the scans on the study's main
308 outcome parameters and the general well-being of the animals have to be considered.

309 In this study, isoflurane was used as anesthetic agent for the *in vivo* micro-CT scans, which is
310 the most commonly used inhalation anesthetic in longitudinal imaging studies with a fast on-
311 and offset of anesthesia and low metabolism rate[17]. Despite its general use, isoflurane has
312 been associated with several adverse effects, such as hepatic degenerative changes[47],
313 immunomodulation[48], oxidative DNA damage[49] as well as alterations in expression profiles of

314 oncogene and tumor suppressor genes in the bone marrow[50], which might potentially also
315 affect fracture healing and the general well-being of the animals. A recent study by
316 Hohlbaum et al. (2017)[17], which assessed the impact of repeated isoflurane anesthesia (6
317 times for 45 min at an interval of 3–4 days) and the associated handling on the well-being of
318 adult C57BL/6JRj mice, categorized the degree of distress as mild according to the EU
319 Directive 2010/63 with only short-term impairment of well-being, mainly in the immediate
320 post-anesthetic period. Therefore, isoflurane-based inhalation anesthesia and the associated
321 handling of the animal is suggested for longitudinal studies with multiple anesthetic sessions
322 per animal.

323 In this study, the applied micro-CT settings (55 kVp, 145 µA, 350 ms integration time, 500
324 projections per 180°, 21 mm field of view (FOV), scan duration ca. 15 min) were adapted
325 from well-established protocols used for longitudinal monitoring of bone adaptation and
326 implant integration in tail vertebrae in mice[14,51]. These settings are similar to protocols used
327 in 2 of the 5 longitudinal fracture healing studies published so far[3,4], while the 3 other
328 studies did not specify the CT settings[2,32,33]. The radiation dosage (CT dose index, CTDI)
329 associated with each scan in the current study was previously estimated to be 0.67 Gy per
330 scan[51,52]. A radiation control experiment using similar settings did not show detrimental
331 effects of 5 weekly *in vivo* micro-CT scans on bone development in tail vertebrae of mice[52].

332 However, some studies in non-fractured bone indicate cumulative radiation-associated
333 effects on bone properties particularly when using high radiation doses (>2G)[19]. The
334 radiation effects also depend on animal age[19,27] and ovariectomy (OVX)[11], with younger and
335 ovariectomized animals being more susceptible to radiation. So far, only one study assessed
336 radiation-associated effects of longitudinal *in vivo* micro-CT on bone healing in a uni-cortical

337 tibia burr-hole defect model, and did not find significant radiation effects on bone
338 properties[1]. In this study, similar CT settings (45kVp, 133 µA, 200 ms integration time, 1000
339 projections per 180°) were used; however, due to the smaller dimensions of the defect and
340 resulting shorter scanning time, the radiation dosage (0.36 Gy) was lower compared to our
341 protocol (0.64 Gy).

342 In the current study, we assessed the combined imaging-associated impact (anesthesia,
343 handling, radiation; 1x/week for 6 weeks) on callus formation and remodeling in a
344 diaphyseal femur defect model in adult female C57BL/6J mice. We did not see any significant
345 imaging-associated changes in bone volume and turnover in the fracture callus during the
346 remodeling phase (post-operative week 5 and 6). Furthermore, no significant differences in
347 callus mineralization between scanned (d0, week1-6) and control animals (d0, week 5+6) in
348 any of the assessed callus volumes (TOT, DC, DP, FP) were observed. The distribution of the
349 osseous callus volume into the three sub-volumes was also not significantly different
350 between groups, indicating similar healing patterns. In addition, when separately assessing
351 the cortical fragments between the inner pins (FC), also no significant differences in any of
352 the assessed parameters were detected between groups. These 3D micro-CT based results
353 were supported by 2D histomorphometric analysis, which also showed no significant
354 differences in tissue composition (bone, cartilage, fibrous tissue, bone marrow) in the former
355 defect region. In respect to clinical healing outcome, the percentage of unions in animals
356 above the sub-critical defect length was 67% in both groups with restoration of the
357 medullary cavity. Defects without cortical bridging only showed small cartilage residuals
358 (<1%) as visualized by Safranin-O staining, indicating manifestation of non-union formation.

359 In the defect regions of unions, no cartilage was seen, indicating progression towards the
360 end of the healing period.

361 So far only few studies have focused on the underlying mechanisms of radiation-induced
362 effects on bone mainly focusing on changes in expression profiles of osteoblast and
363 osteoclast differentiation markers[30,35]. Recently, three consecutive *in vivo* studies by
364 Chandra et al.[36,53,54] showed, that radiation-induced bone loss[53,54] is mediated via Sclerostin
365 inhibition of osteoanabolic Wnt-signaling[36]. First, they showed that focal radiation increases
366 Sclerostin expression in trabecular bone in mice. Using a Sclerostin antibody, they were then
367 able to block the radiation-induced deterioration in structural bone properties and
368 consistently, trabecular bone in Sclerostin null mice was resistant to radiation. Based on
369 these comprehensive analyses, we also assessed Sclerostin by immunohistochemistry, but
370 did not see any differences in number of stained osteocytes, staining intensity and pattern
371 between the scan and the control group in any of the assessed callus regions.

372 In summary, we did not see significant differences in a total of 10 assessed CT and
373 histological parameters in the total volume (TOT) between the inner pins of the fixator as
374 well as in the different callus sub-volumes (DC, DP, FP) and the adjacent cortical fragments
375 (FC) between the scan and the control group. The sub-volume specific analysis also allowed
376 capturing of distinct features only present in one region (e.g. significant post-operative
377 increase in bone resorption in FC), that showed contrary progression compared to the
378 overall picture (significant post-operative increase in bone formation in DC, DP and FP). This
379 also shows the importance of VOI selection. The other longitudinal fracture healing studies
380 either assessed a VOI consisting of the defect as well as adjacent bone fragments, or then
381 only the callus in the defect region including the last slice of intact cortex[2,3], or the callus in

382 the defect and periosteal region combined[4] was evaluated. An overall VOI including the
383 defect region and cortical fragments can give an overview of callus characteristics, but sub-
384 volume-specific differences might be missed. Therefore, analysis of different endosteal and
385 periosteal callus regions as well as the adjacent cortical volume is favorable.

386 The current study has several limitations. We based our evaluation of longitudinal time-
387 lapsed *in vivo* imaging for monitoring fracture healing on micro-CT and histological
388 assessment of callus properties. Histomorphometry confirmed the micro-CT results.
389 However, contouring of non-union defects is challenging and might be user dependent as
390 indicated previously[55]. This could be addressed in future studies by implementing 2D-3D
391 registration approaches[56], allowing to transfer the automatically computed VOI borders
392 generated for the micro-CT evaluation to the 2D histology analyses. We did not assess
393 systemic effects associated with the repeated *in vivo* micro-CT measurements and isoflurane
394 anesthesia. Due to the required post-operative scan defined in our ethical license, we did
395 not include a second control group only receiving one micro-CT measurement at the
396 endpoint. In respect to the underlying mechanisms associated with radiation effects on
397 fracture healing, we chose to assess Sclerostin by immunohistochemistry, due to the
398 comprehensive available literature. As proposed by Chandra et al.[36], future studies could
399 extend the analysis to other Wnt signaling inhibitors (e.g. DKK1) with the potential to find
400 further targets for prevention of radiation-mediated bone loss. As we only included female
401 animals in the study, our findings could be affected by the estrous cycle of the animals,
402 which in future could be addressed by staging of the cycle using vaginal smears[57]. We
403 minimized the risk of cycle-associated variance by using individual ventilated cages, which
404 have been associated with the Lee–Boot effect (suppression or prolongation of estrous

405 cycles) in group-housed adult female mice isolated from male animals[58]. In addition, recent
406 literature indicates that unstaged female rodents are no more variable than males (revised
407 in [59]).

408 Despite these limitations, the longitudinal *in vivo* micro-CT based approach established in
409 this study allows monitoring of the different healing phases in mouse femur defect models
410 without significant anesthesia-, handling- and radiation-associated effects on callus
411 properties. By registering consecutive scans of the defect region for each animal and
412 implementing a two-threshold approach, data on bone turnover and mineralization kinetics
413 can be obtained, which is important for targeting impaired callus remodeling under different
414 conditions (e.g. premedication with bisphosphonates) with pharmacological and mechanical
415 therapies. Importantly, repeated anesthesia, handling and radiation associated with the
416 scans did not impair callus formation and remodeling. Therefore, this study supports the
417 application of longitudinal *in vivo* micro-CT for healing-phase specific monitoring of fracture
418 repair in mice. Further studies should evaluate the potential of this micro-CT-based
419 monitoring approach for healing phase-specific discrimination of normal and impaired
420 healing conditions.

421

422 **Methods**

423 **Study design**

424 A micro-CT based approach for longitudinal *in vivo* monitoring of fracture healing was
425 established for a mouse femur defect model (for details on study design see Supplementary
426 Table S1 online). All mice received a femur defect and post-operative micro-CT scans (vivaCT
427 40, ScancoMedical, Brüttisellen, Switzerland) were performed. The scan group then received

428 weekly scans of the defect area (weeks 1-6). To assess the combined effect of radiation,
429 anesthesia and handling associated with weekly micro-CT measurements, controls were only
430 scanned after 5 weeks. Control animals then received another scan in post-operative week 6
431 to enable the assessment of both, static and dynamic bone parameters during the final
432 remodeling phase of fracture healing.
433
434 **Animals**
435 All animal procedures were approved by the authorities (licence number: 36/2014;
436 Kantonales Veterinäramt Zürich, Zurich, Switzerland). We confirm that all methods were
437 carried out in accordance with relevant guidelines and regulations (ARRIVE guidelines and
438 Swiss Animal Welfare Act and Ordinance (TSchG, TSchV)). To study adult fracture healing
439 female 12 week-old C57BL/6J mice were purchased from Janvier (Saint Berthevin Cedex,
440 France) and housed in the animal facility of the ETH Phenomics Center (EPIC; 12h:12h light-
441 dark cycle, maintenance feed (3437, KLIBA NAFAG, Kaiseraugst, Switzerland), 5
442 animals/cage) for 8 weeks. At an age of 20 weeks, all animals received a femur defect by
443 performing an osteotomy (group 1: control group, defect length - 1.45mm ± 0.16, n=8; group
444 2: scan group, defect length -1.47mm ± 0.16, n=11; housing after surgery: 2-3 animals/cage;
445 for details on study design see Supplementary Table 1 online). All defect surgeries were
446 performed by the same veterinarian. Perioperative analgesia (25 mg/L, Tramal®,
447 Gruenenthal GmbH, Aachen, Germany) was provided via the drinking water two days before
448 surgery until the third post-operative day. For surgery and micro-CT scans, animals were
449 anesthetized with isoflurane (induction/maintenance: 5%/1-2% isoflurane/oxygen).

450 Perioperative handling and monitoring was performed by the surgeon and one other
451 veterinarian.
452
453 **Femur osteotomy**
454 In all animals an external fixator (Mouse ExFix, RISystem, Davos, Switzerland; stiffness:
455 24N/mm) was positioned at the craniolateral aspect of the right femur and attached using
456 four mounting pins. First, the most distal pin was inserted approximately 2mm proximal to
457 the growth plate, followed by placement of the most proximal and the inner pins.
458 Subsequently, a femur defect was created using 2 Gigli wire saws.
459
460 **Time-lapsed *in vivo* micro-CT**
461 Immediate post-surgery correct positioning of the fixator and the defect was visualized using
462 a vivaCT 40 (Scanco Medical AG, Brüttisellen, Switzerland) (isotropic nominal resolution: 10.5
463 µm; 2 stacks of 211 slices; 55 kVp, 145 µA, 350 ms integration time, 500 projections per
464 180°, 21 mm field of view (FOV), scan duration ca. 15 min). Subsequently, the fracture callus
465 and the adjacent bone between the inner pins of the fixator were scanned weekly using the
466 same settings. Scans were registered consecutively using a branching scheme (registration of
467 whole scan for bridged defects; separate registration of the two fragments for unbridged
468 defects)[5]. Subsequently, morphometric indices (bone volume - BV, bone volume/total
469 volume – BV/TV, bone formation rate – BFR, bone resorption rate - BRR) were computed
470 (threshold: 395mg HA/cm^3; for details on methods see [5]). To assess mineralization
471 progression, a second threshold (645mg HA/cm^3) was applied and the ratio between highly
472 and lowly mineralized tissue (BV_{645}/BV_{395}) was calculated. The two selected thresholds are

473 included in our recently developed multidensity threshold approach[5]. Similar thresholds
474 have previously been used in fracture healing studies[60,61]. The lower threshold (395mg
475 HA/cm^3) was selected to capture early callus formation, based on its previous application for
476 assessment of lowly mineralized tissue in the metabolically active trabecular
477 compartment[62,63]. The choice of the second threshold (645 mg HA/cm^3) for monitoring callus
478 mineralization was based on thresholds previously applied to well-mineralized cortical
479 bone[62,63]. It has to be considered, that micro-CT-based assessment of the mineralization
480 process is known to be affected by the polychromatic cone beam (≤10% error in the
481 quantification of the local bone mineral density[64]). We used an aluminium filter to further
482 reduce the effect of beam hardening[65] and applied scanning settings previously evaluated
483 for monitoring *in vivo* mineralization kinetics[66]. According to the standard clinical evaluation
484 of X-rays, the number of bridged cortices per callus was evaluated in two perpendicular
485 planes (UCT Evaluation V6.5-1, Scanco Medical AG, Brüttisellen, Switzerland). A ''healed
486 fracture'' was considered as having a minimum of at least three bridged cortices per callus.
487 For evaluation, four volumes of interest (VOIs) were defined, which were created
488 automatically from the post-operative measurement (Fig. 1): defect center (DC), defect
489 periphery (DP), cortical fragment center (FC), and fragment periphery (FP). Data were
490 normalised to the central VOIs: DC/DC, DP/DC, FC/FC, FP/FC.
491
492 **Histology**
493 Histological analyses were performed in a sub-set of animals (n=6/group). On day 42, femora
494 were excised, the femoral head was removed and the samples were placed in 4% neutrally
495 buffered formalin for 24 hours and subsequently decalcified in 12.5% EDTA for 10-14 days.

496 The samples were embedded in paraffin and 4.5 µm longitudinal sections were stained with
497 Safranin-O/Fast Green: Weigert's iron haematoxylin solution (HT1079, Sigma-Aldrich, St.
498 Louis, MO) - 4min, 1:10 HCl-acidified 70% ethanol - 10s, tap water - 5min, 0.02% Fast Green
499 (F7258, Sigma-Aldrich, St. Louis, MO) - 3min, 1% acetic acid - 10s, 0.1% Safranin-O (84120,
500 Fluka, St. Louis, MO) - 5min. Images were taken with Slide Scanner Pannoramic 250 (3D
501 Histech, Budapest, Hungary) at 20x magnification.
502
503 For immunohistochemical staining of Sclerostin, nonspecific sites were blocked (1% BSA/PBS
504 + 1% rabbit serum) for 60 min at room temperature. Subsequently, the sections were
505 incubated with the primary antibody against Sclerostin (AF1589, R&D Systems, Minneapolis,
506 MN; 1:150 in 1%BSA/PBS + 0.2% rabbit serum) overnight at 4°C. To detect the primary
507 antibody, a secondary biotinylated rabbit anti-goat-IgG antibody (BAF017, R&D Systems,
508 Minneapolis, MN) was added for 1 h at room temperature. For signal amplification, the
509 slides were incubated with avidin-biotin complex (PK-6100 Vector Laboratories, Burlingame,
510 CA) for 30 min. Diaminobenzidine (Metal Enhanced DAB Substrate Kit, 34065 ThermoFisher
511 Scientific, Waltham, MA) was used as detection substrate. Counterstaining was performed
512 with FastGreen (F7258, Sigma-Aldrich, St. Louis, MO). Species-specific IgG was used as
513 isotype control. Images were taken with Slide Scanner Pannoramic 250 (3D Histech,
514 Budapest, Hungary) at 40x magnification.
515
516 For histomorphometric analysis, the callus and adjacent cortical fragments between the
517 inner pins of the fixator were manually contoured on Safranin-O stained sections and the
518 tissue area of this region of interest (ROI) was quantified using commercial software

519 (n=6/group; Fiji[67]). Similarly, the different tissue types (bone, cartilage, fibrous tissue and
520 bone marrow) in the ROI were manually contoured and quantified.
521
522 **Statistics**
523 CT analysis and histomorphometry: Data were tested for normal distribution (Shapiro-Wilk-
524 Test) and homogeneity of variance (Levene-Test). Depending on the test outcome, group
525 comparisons (scan versus control group) of data derived at single time points were
526 performed by two-tailed Student's t-test or Mann-Whitney U-test (IBM SPSS Statistics
527 Version 23). For statistical evaluation of repeated measurements (scan group) dependent on
528 results from normality and variance tests, either one-way analysis of variance (ANOVA) with
529 Bonferroni correction or Friedman test with Dunn correction for multiple comparisons
530 (GraphPad Prism 7) were performed. Two-way ANOVA was used for longitudinal comparison
531 of the body weight between the control and the scan group. The level of significance was set
532 at $p < 0.05$.
533
534 **Acknowledgements**
535 The authors gratefully acknowledge support from the EU (BIODESIGN FP7-NMP-2012-
536 262948 and ERC Advanced MechAGE ERC-2016-ADG-741883). E. Wehrle received funding
537 from the ETH Postdoctoral Fellowship Program (MSCA-COFUND, FEL-25_15-1).
538
539 **Author Contributions Statement**

The study was designed by E.W., G.A.K., S.H. and R.M.. The experiments were performed by E.W., G.A.K. and A.C.S.. Data analyses were performed by E.W. and D.C.B.. The manuscript was written by E.W. and reviewed and approved by all authors.

Data availability

All necessary data generated or analyzed during the present study are included in this published article and its Supplementary Information files (preprint available on BioRxiv (BIORXIV/2019/692343). Additional information related to this paper may be requested from the authors.

Competing Interests

The authors declare no competing interests.

References

1 Taiani, J. T. *et al.* Embryonic stem cell therapy improves bone quality in a model of impaired fracture healing in the mouse; tracked temporally using in vivo micro-CT. *Bone* **64**, 263-272 (2014).

2 Locher, R. J. *et al.* Traumatic brain injury and bone healing: radiographic and biomechanical analyses of bone formation and stability in a combined murine trauma model. *J. Musculoskel. Neuron.* **15**, 309-315 (2015).

3 Graef, F. *et al.* Impaired fracture healing with high non-union rates remains irreversible after traumatic brain injury in leptin-deficient mice. *J. Musculoskel. Neuron.* **17**, 78-85 (2017).

4 Mehta, M., Checa, S., Lienau, J., Hutmacher, D. & Duda, G. N. In vivo tracking of segmental bone defect healing reveals that callus patterning is related to early mechanical stimuli. *Eur. Cell Mater.* **24**, 358-371 (2012).

5 Tourolle né Betts, D. C. *et al.* The association between mineralised tissue formation and the mechanical local in vivo environment: Time-lapsed quantification of a mouse defect healing model. Preprint at https://doi.org/10.1101/721365 (2019).

6 Hauser, M., Siegrist, M., Keller, I. & Hofstetter, W. Healing of fractures in osteoporotic bones in mice treated with bisphosphonates - A transcriptome analysis. *Bone* **112**, 107-119 (2018).

7 Bao, Q. W. *et al.* An appropriate Wnt/beta-catenin expression level during the remodeling phase is required for improved bone fracture healing in mice. *Sci. Rep.-Uk* **7**, doi:ARTN 269510.1038/s41598-017-02705-0 (2017).

8 Hegde, V., Jo, J. E., Andreopoulou, P. & Lane, J. M. Effect of osteoporosis medications on fracture healing. *Osteoporosis Int* **27**, 861-871 (2016).

9 Schindeler, A., McDonald, M. M., Bokko, P. & Little, D. G. Bone remodeling during fracture repair: The cellular picture. *Semin. Cell. Dev. Biol.* **19**, 459-466 (2008).

10 Boyd, S. K., Davison, P., Muller, R. & Gasser, J. A. Monitoring individual morphological changes over time in ovariectomized rats by in vivo micro-computed tomography. *Bone* **39**, 854-862 (2006).

11 Klinck, R. J., Campbell, G. M. & Boyd, S. K. Radiation effects on bone architecture in mice and rats resulting from in vivo micro-computed tomography scanning. *Med. Eng. Phys.* **30**, 888-895 (2008).

12 Lambers, F. M., Kuhn, G., Schulte, F. A., Koch, K. & Muller, R. Longitudinal Assessment of In Vivo Bone Dynamics in a Mouse Tail Model of Postmenopausal Osteoporosis. *Calcified Tissue Int.* **90**, 108-119 (2012).

13 David, V. *et al.* Noninvasive in vivo monitoring of bone architecture alterations in hindlimb-unloaded female rats using novel three-dimensional microcomputed tomography. *J. Bone Miner. Res.* **18**, 1622-1631 (2003).

14 Lambers, F. M., Schulte, F. A., Kuhn, G., Webster, D. J. & Muller, R. Mouse tail vertebrae adapt to cyclic mechanical loading by increasing bone formation rate and decreasing bone resorption rate as shown by time-lapsed in vivo imaging of dynamic bone morphometry. *Bone* **49**, 1340-1350 (2011).

15 Schulte, F. A., Lambers, F. M., Kuhn, G. & Muller, R. In vivo micro-computed tomography allows direct three-dimensional quantification of both bone formation and bone resorption parameters using time-lapsed imaging. *Bone* **48**, 433-442 (2011).

16 Kuhn, G., Weigt, C., Lambers, F. M., Schulte, F. A. & Muller, R. Bisphosphonate treatment does not impair load adaptation in osteopenic mouse bones. *Bone* **50**, S156-S156 (2012).

17 Hohlbaum, K. *et al.* Severity classification of repeated isoflurane anesthesia in C57BL/6JRj mice-Assessing the degree of distress. *Plos One* **12**, doi:ARTN e017958810.1371/journal.pone.0179588 (2017).

18 Tremoleda, J. L. *et al.* Imaging technologies for preclinical models of bone and joint disorders. *Ejnmmi Res* **1**, doi:Artn 1110.1186/2191-219x-1-11 (2011).

19 Laperre, K. *et al.* Development of micro-CT protocols for in vivo follow-up of mouse bone architecture without major radiation side effects. *Bone* **49**, 613-622 (2011).

20 Hildebrandt, I. J., Su, H. & Weber, W. A. Anesthesia and other considerations for in vivo imaging of small animals. *ILAR J* **49**, 17-26 (2008).

21 Mustafy, T., Benoit, A., Londono, I., Moldovan, F. & Villemure, I. Can repeated in vivo micro-CT irradiation during adolescence alter bone microstructure, histomorphometry and longitudinal growth in a rodent model ? *Plos One* **13**, doi:ARTN e020732310.1371/journal.pone.027323 (2018).

22 Richardson, C. A. & Flecknell, P. A. Anaesthesia and post-operative analgesia following experimental surgery in laboratory rodents: Are we making progress? *Atla-Altern. Lab Anim.* **33**, 119-127 (2005).

23 Dudziak, M. E. *et al.* The effects of ionizing radiation on osteoblast-like cells in vitro. *Plast. Reconstr. Surg.* **106**, 1049-1061 (2000).

24 Matsumura, S., Jikko, A., Hiranuma, H., Deguchi, A. & Fuchihata, H. Effect of X-ray irradiation on proliferation and differentiation of osteoblast. *Calcif. Tissue Int.* **59**, 307-308 (1996).

25 Scheven, B. A. A., Burger, E. H., Kawilarangdehaas, E. W. M., Wassenaar, A. M. & Nijweide, P. J. Effects of Ionizing Irradiation on Formation and Resorbing Activity of Osteoclasts In vitro. *Lab. Invest.* **53**, 72-79 (1985).

26 Brouwers, J. E. M., Van Rietbergen, B. & Huiskes, R. No effects of in vivo micro-CT radiation on structural parameters and bone marrow cells in proximal tibia of Wistar rats detected after eight weekly scans. *J. Orthop. Res.* **25**, 1325-1332 (2007).
27 Willie, B. M. *et al.* Diminished response to in vivo mechanical loading in trabecular and not cortical bone in adulthood of female C57Bl/6 mice coincides with a reduction in deformation to load. *Bone* **55**, 335-346 (2013).
28 Jegoux, F., Malard, O., Goyenvalle, E., Aguado, E. & Daculsi, G. Radiation effects on bone healing and reconstruction: interpretation of the literature. *Oral Surg. Oral Med.* **109**, 173-184 (2010).
29 Donneys, A. *et al.* Deferoxamine Restores Callus Size, Mineralization, and Mechanical Strength in Fracture Healing after Radiotherapy. *Plast. Reconstr. Surg.* **131**, 711e-719e (2013).
30 Chen, M. *et al.* Low-Dose X-Ray Irradiation Promotes Osteoblast Proliferation, Differentiation and Fracture Healing. *Plos One* **9**, doi:ARTN e10401610.1371/journal.pone.0104016 (2014).
31 Wu, Y. R. *et al.* External Beam Irradiation Preferentially Inhibits the Endochondral Pathway of Fracture Healing: A Rat Model. *Clin. Orthop. Relat. R.* **476**, 2076-2090 (2018).
32 Tsitsilonis, S. *et al.* The effect of traumatic brain injury on bone healing: an experimental study in a novel in vivo animal model. *Injury* **46**, 661-665 (2015).
33 Wang, A. Y. *et al.* Effect of cervus and cucumis peptides on osteoblast activity and fracture healing in osteoporotic bone. *Evid. Based Compl. Alt.* **2014**, 958908 (2014).
34 O'Donovan, D. A. *et al.* Radiation-Induced Craniofacial Bone Growth Inhibition: Acute and Long-Term Effects on Bone Histopathology with and without Cytoprotection. *Plast. Reconstr. Surg* **129**, 636e-645e (2012).
35 Zhang, J. *et al.* Differences in responses to X-ray exposure between osteoclast and osteoblast cells. *J. Radiat. Res.* **58**, 791-802 (2017).
36 Chandra, A. *et al.* Suppression of Sclerostin Alleviates Radiation-Induced Bone Loss by Protecting Bone-Forming Cells and Their Progenitors Through Distinct Mechanisms. *Journal of Bone and Mineral Research* **32**, 360-372 (2017).
37 Borgiani, E. *et al.* Age-Related Changes in the Mechanical Regulation of Bone Healing Are Explained by Altered Cellular Mechanoresponse. *J. Bone Miner. Res.*, doi:10.1002/jbmr.3801 (2019).
38 Kruck, B. *et al.* Sclerostin Neutralizing Antibody Treatment Enhances Bone Formation but Does Not Rescue Mechanically Induced Delayed Healing. *J. Bone Miner. Res.* **33**, 1686-1697 (2018).
39 Bundkirchen, K. *et al.* Hemorrhagic shock alters fracture callus composition and activates the IL6 and RANKL/OPG pathway in mice. *J. Trauma Acute Care* **85**, 359-366 (2018).
40 Jilka, R. L. The Relevance of Mouse Models for Investigating Age-Related Bone Loss in Humans. *J. Gerontol. a-Biol* **68**, 1209-1217 (2013).
41 Miyagawa, K. *et al.* A novel underuse model shows that inactivity but not ovariectomy determines the deteriorated material properties and geometry of cortical bone in the tibia of adult rats. *J. Bone Miner. Metab.* **29**, 422-436 (2011).
42 Lotinun, S. *et al.* Osteoclast-specific cathepsin K deletion stimulates S1P-dependent bone formation. *J. Clin. Invest.* **123**, 666-681 (2013).
43 Birkhold, A. I. *et al.* The Periosteal Bone Surface is Less Mechano-Responsive than the Endocortical. *Sci. Rep.-Uk* **6**, doi:ARTN 2348010.1038/srep23480 (2016).
44 Zwingenberger, S. *et al.* Establishment of a femoral critical-size bone defect model in immunodeficient mice. *J. Surg. Res.* **181**, e7-e14 (2013).
45 Russel, W. M. S. & Burch, R. L. *The Principles of Humane Experimental Technique* (1959).
46 Tannenbaum, J. & Bennett, B. T. Russell and Burch's 3Rs Then and Now: The Need for Clarity in Definition and Purpose. *J. Am. Assoc. Lab. Anim.* **54**, 120-132 (2015).

47 Stevens, W. C. *et al.* Comparative Toxicities of Halothane, Isoflurane, and Diethyl-Ether at Subanesthetic Concentrations in Laboratory-Animals. *Anesthesiology* **42**, 408-419 (1975).
48 Stollings, L. M. *et al.* Immune Modulation by Volatile Anesthetics. *Anesthesiology* **125**, 399-411 (2016).
49 Kim, H. *et al.* Oxidative damages in the DNA, lipids, and proteins of rats exposed to isofluranes and alcohols. *Toxicology* **220**, 169-178 (2006).
50 Kadar, B. *et al.* Effects of isoflurane exposure on oncogene and tumour suppressor gene expressions in vital organs of CBA/CA mice. *In Vivo* **21**, 861-865 (2007).
51 Li, Z. H., Kuhn, G., Schirmer, M., Muller, R. & Ruffoni, D. Impaired bone formation in ovariectomized mice reduces implant integration as indicated by longitudinal in vivo micro-computed tomography. *Plos One* **12**, doi:ARTN e018483510.1371/journal.pone.0184835 (2017).
52 Lambers, F. M. *et al.* Bone adaptation to cyclic loading in murine caudal vertebrae is maintained with age and directly correlated to the local micromechanical environment. *J. Biomech.* **48**, 1179-1187 (2015).
53 Chandra, A. *et al.* PTH prevents the adverse effects of focal radiation on bone architecture in young rats. *Bone* **55**, 449-457 (2013).
54 Chandra, A. *et al.* PTH1-34 alleviates radiotherapy-induced local bone loss by improving osteoblast and osteocyte survival. *Bone* **67**, 33-40 (2014).
55 Freeman, T. A., Patel, P., Parvizi, J., Antoci, V. & Shapiro, I. M. Micro-CT Analysis with Multiple Thresholds Allows Detection of Bone Formation and Resorption during Ultrasound-Treated Fracture Healing. *J. Orthop. Res.* **27**, 673-679 (2009).
56 Taylor, C., Scheuren, A., Trüssel, A. & R., M. 3D local in vivo environment (LivE) imaging for single cell protein analysis of bone tissue. *Curr. Dir. Biomed. Eng.* **2**, 449-453 (2016).
57 Hofman, M. *et al.* Effect of neurokinin-1-receptor blockage on fracture healing in rats. *Sci. Rep.-Uk* **9**, doi:ARTN 974410.1038/s41598-019-46278-6 (2019).
58 Nevalainen, T. Animal Husbandry and Experimental Design. *Ilar Journal* **55**, 392-398 (2014).
59 Beery, A. K. Inclusion of females does not increase variability in rodent research studies. *Curr. Opin. Behav. Sci.* **23**, 143-149 (2018).
60 O'Neill, K. R. *et al.* Micro-computed tomography assessment of the progression of fracture healing in mice. *Bone* **50**, 1357-1367 (2012).
61 Morgan, E. F. *et al.* Micro-computed tomography assessment of fracture healing: Relationships among callus structure, composition, and mechanical function. *Bone* **44**, 335-344 (2009).
62 Wehrle, E. *et al.* Distinct Frequency Dependent Effects of Whole-Body Vibration on Non-Fractured Bone and Fracture Healing in Mice. *J. Orthop. Res.* **32**, 1006-1013 (2014).
63 Wehrle, E. *et al.* The impact of low-magnitude high-frequency vibration on fracture healing is profoundly influenced by the oestrogen status in mice. *Dis. Model. Mech.* **8**, 93-104 (2015).
64 Mulder, L., Koolstra, J. H. & Van Euden, T. M. G. J. Accuracy of MicroCT in the quantitative determination of the degree and distribution of mineralization in developing bone. *Acta Radiol.* **45**, 769-777 (2004).
65 Meganck, J. A., Kozloff, K. M., Thornton, M. M., Broski, S. M. & Goldstein, S. A. Beam hardening artifacts in micro-computed tomography scanning can be reduced by X-ray beam filtration and the resulting images can be used to accurately measure BMD. *Bone* **45**, 1104-1116 (2009).
66 Lukas, C. *et al.* Mineralization kinetics in murine trabecular bone quantified by time-lapsed in vivo micro-computed tomography. *Bone* **56**, 55-60 (2013).
67 Schindelin, J. *et al.* Fiji: an open-source platform for biological-image analysis. *Nat. Methods* **9**, 676-682, doi:10.1038/Nmeth.2019 (2012).

721 **Figure Legends**

722 **Figure 1.** Volumes of interest (VOIs) for micro-CT evaluation of callus and adjacent bone:
723 Defect center (DC - red), defect periphery (DP - yellow), fragment center (FC - blue),
724 fragment periphery (FP - orange).

725

726 **Figure 2.** Representative images (full image and cut; threshold: 645 mg HA/cm^3) of the
727 defect region from animals of the scan group (week 0-6): union defect (top panel), non-
728 union defect (bottom panel). Visualization of bone formation (orange) and resorption (blue)
729 via registration of micro-CT scans from week 5 and 6.

730

731 **Figure 3**. Micro-CT based evaluation of bone parameters in the scan group using different
732 VOIS: total VOI (TOT) - defect and adjacent bone fragments (top), defect VOI (DC+DP) –
733 defect center and periphery (bottom). a+d. Bone formation rate (solid) and bone resorption
734 rate (dashed line) in the femur defect (TV) given in percent per day. b+e: Bone volume (BV)
735 normalized to TV (DC+FC for TOT and DC for DC+DP). c+f: Degree of bone mineralization
736 given as ratio of bone volume with a density ≥645 mg HA/cm^3 to the total osseous volume in
737 the defect (threshold ≥395 mg HA/cm^3). n=10; * indicates $p < 0.05$ between consecutive
738 weeks determined by Friedman test with Dunn correction for multiple comparisons (a-e)/
739 repeated measurements ANOVA with Bonferroni correction (f).

740

741 **Figure 4.** Micro-CT based evaluation of bone parameters in the scan (red) and control group
742 (blue) using different VOIS: total VOI (TOT: DC+DP+FC+FP) - defect and adjacent bone
743 fragments (top), defect VOI (DC+DP) – defect center and periphery (bottom). a+d. Formed
744 (solid) and resorbed (empty) bone volume (BV) in the femur defect (TV) given in percent per

745 day. b+e: Bone volume (BV) normalized to TV (DC+FC for TOT and DC for DC+DP). c+f:
746 Degree of bone mineralization given as ratio of bone volume with a density ≥645 mg HA/cm^3
747 to the total osseous volume in the defect (threshold ≥395 mg HA/cm^3). Control group: n=8,
748 scan group: n=10. * indicates $p < 0.05$ determined by two-tailed Student's t-test (a-e; f: week
749 6)/Mann-Whitney U-test (f: week 5).

750

751 **Figure 5.** Representative longitudinal sections of fractured femora 6 weeks after defect
752 surgery of unions and non-unions in the scan and control group. Top panel: Safranin-O
753 staining - overview images (row 1), scale bar = 2 mm; area between inner pins of fixator (row
754 2), scale bar = 500 µm; bottom panel: Sclerostin staining – area centered between inner pins
755 of fixator (row 3), scale bar = 100 µm; Isotype control for Sclerostin staining (row 4), scale
756 bar = 100 µm.

757

758 **Tables**

759 **Table 1.** Micro-CT based evaluation of bone parameters in the scan group using different VOIS

		Post-operative week								Post-operative week							
		0-1	1-2	2-3	3-4	4-5	5-6	p-value #		0	1	2	3	4	5	6	p-value #
DC	BFR [%/day]	0.23 ± 0.10*	2.24 ± 1.20	2.40 ± 1.15	1.30 ± 0.49	0.63 ±0.14	0.41 ± 0.09	< 0.0001	BV/TV [%]	1 ± 0	3 ± 1	17 ± 9*	28 ± 15	30 ± 14	29 ± 12	28 ± 10	< 0.0001
	BRR [%/day]	0.06 ± 0.02	0.14 ± 0.04*	0.88 ± 0.36	1.06 ± 0.85	0.75 ± 0.43	0.52 ± 0.25	< 0.0001	BV_{645}/BV_{395} [%]	1 ± 1	34 ± 10	26 ± 6	49 ± 7	67 ± 6	76 ± 6	80 ± 6	< 0.0001
DP	BFR [%/day]	0.03 ± 0.02*	0.38 ± 0.16	1.07 ± 0.88	0.68 ± 0.52	0.28 ± 0.20	0.18 ± 0.11	< 0.0001	BV/TV [%]	0 ± 0	0 ± 0	3 ± 1	9 ± 7	11 ± 9	11 ± 9	11 ± 8	< 0.0001
	BRR [%/day]	0.01 ± 0.0	0.03 ± 0.02	0.19 ± 0.08	0.34 ± 0.31	0.30 ± 0.23	0.18 ± 0.16	< 0.0001	BV_{645}/BV_{395} [%]	2 ± 3	24 ± 11	8 ± 2	37 ± 9	61 ± 10	71 ± 7	74 ± 9	< 0.0001
FC	BFR [%/day]	0.22 ± 0.08	0.26 ± 0.15	0.31 ± 0.12	0.44 ± 0.19	0.45 ± 0.11	0.40 ± 0.12	0.0019	BV/TV [%]	57 ± 7	57 ± 6	53 + 6	48 ± 5	44 ± 5	41 ± 6	40 ± 7	< 0.0001
	BRR [%/day]	0.24 ± 0.17*	0.78 ± 0.31	1.13 ± 0.30	1.01 ± 0.30	0.80 ± 0.25	0.60 ± 0.21	< 0.0001	BV_{645}/BV_{395} [%]	95 ± 1	92 ± 1	89 ±2	87 ± 1	86 ± 2	86 ± 2	86 ± 3	< 0.0001
FP	BFR [%/day]	0.43 ± 0.09*	1.81 ± 0.58	1.77 ± 0.76	0.85 ± 0.41	0.51 ± 0.28	0.33 ± 0.20	< 0.0001	BV/TV [%]	5 ± 1	6 ± 1	16 ± 4	21 ± 7	20 ± 8	20 ± 9	20 ± 9	< 0.0001
	BRR [%/day]	0.20 ± 0.09	0.40 ± 0.13*	1.16 ± 0.30	0.90 ± 0.38	0.57 ± 0.22	0.35 ± 0.14	< 0.0001	BV_{645}/BV_{395} [%]	0 ± 0	34 ± 9	23 ± 7	52 ± 7	69 ± 5	75 ± 4	78 ± 3	< 0.0001

760 DC = defect center, DP = defect periphery, FC = cortical fragment center, FP = cortical fragment periphery; BFR – bone formation rate; BRR – bone resorption rate; BV/TV - bone
761 volume normalized to DC for DC, DP and FC for FC, FP; BV645/BV395 - degree of bone mineralization given as ratio of bone volume with a density ≥645 mg HA/cm^3 to the total
762 osseous volume (threshold: 395mg HA/cm^3); *, significant difference compared to subsequent week ($p < 0.05$); #, p-value over time as tested with repeated measurements
763 ANOVA with Bonferroni correction/Friedman test with Dunn correction for multiple comparisons, n=10

764 **Table 2.** CT evaluation of bone parameters in the different volumes of interest (VOI) for the
765 scan and control group

VOI	Parameter	Evaluation time point/period	Control group	Scan group
DC	BFR [%/day]	week 5-6	0.59 ± 0.24	0.41 ± 0.09
	BRR [%/day]	week 5-6	0.62 ± 0.28	0.52 ± 0.25
	BV/TV [%]	week 5	35 ± 11	29 ± 12
		week 6	35 ± 11	28 ± 10
	BV_{645}/BV_{395} [%]	week 5	76 ± 2	76 ± 6
		week 6	80 ± 3	80 ± 6
DP	BFR [%/day]	week 5-6	0.18 ± 0.12	0.18 ± 0.11
	BRR [%/day]	week 5-6	0.15 ± 0.11	0.18 ± 0.16
	BV/TV [%]	week 5	11 ± 8	11 ± 9
		week 6	11 ± 8	11 ± 8
	BV_{645}/BV_{395} [%]	week 5	71 ± 7	71 ± 7
		week 6	75 ± 6	74 ± 9
FC	BFR [%/day]	week 5-6	0.44 ± 0.19	0.40 ± 0.12
	BRR [%/day]	week 5-6	0.63 ± 0.19	0.60 ± 0.21
	BV/TV [%]	week 5	42 ± 6	41 ± 6
		week 6	41 ± 6	40 ± 7
	BV_{645}/BV_{395} [%]	week 5	84 ± 3	86 ± 2
		week 6	84 ± 3	86 ± 3
FP	BFR [%/day]	week 5-6	0.32 ± 0.09	0.33 ± 0.20
	BRR [%/day]	week 5-6	0.30 ± 0.09	0.35 ± 0.14
	BV/TV [%]	week 5	21 ± 8	20 ± 9
		week 6	21 ± 8	20 ± 9
	BV_{645}/BV_{395} [%]	week 5	76 ± 5	75 + 4
		week 6	79 ± 4	78 + 3

766 DC - defect center; DP - defect periphery; FC – fragment center; FP – fragment periphery; BFR – bone
767 formation rate; BRR – bone resorption rate; BV/TV - bone volume normalized to DC for DC, DP and FC
768 for FC, FP. BV_{645}/BV_{395} - degree of bone mineralization given as ratio of bone volume with a density
769 ≥645 mg HA/cm^3 to the total osseous volume (threshold: 395mg HA/cm^3). Control/scan group -
770 n=8/10; no significant differences were detected between the scan group and the control group ($p \geq$
771 0.05), assessed by two-tailed Student's t-test or Mann-Whitney U-test.

Table 3. Number of bridged cortices per callus evaluated in two perpendicular planes and number of mice with successful fracture healing (≥ 3 bridged cortices) evaluated 5 and 6 weeks after the defect surgery.

	Number of bridged cortices					Fracture healing outcome[#]	
Group	0	1	2	3	4	Not healed	Healed
Scan							
all animals	3	0	1	0	7	4 (36%)	7 (64%)
defects ≥ 1.5mm	3	0	1	0	2	4 (67%)	2 (33%)
Control							
all animals	2	0	0	0	6	2 (25%)	6 (75%)
defects ≥ 1.5mm	2	0	0	0	1	2 (67%)	1 (33%)

[#], percentages of healed/not healed fractures per group given in brackets

Figure 1

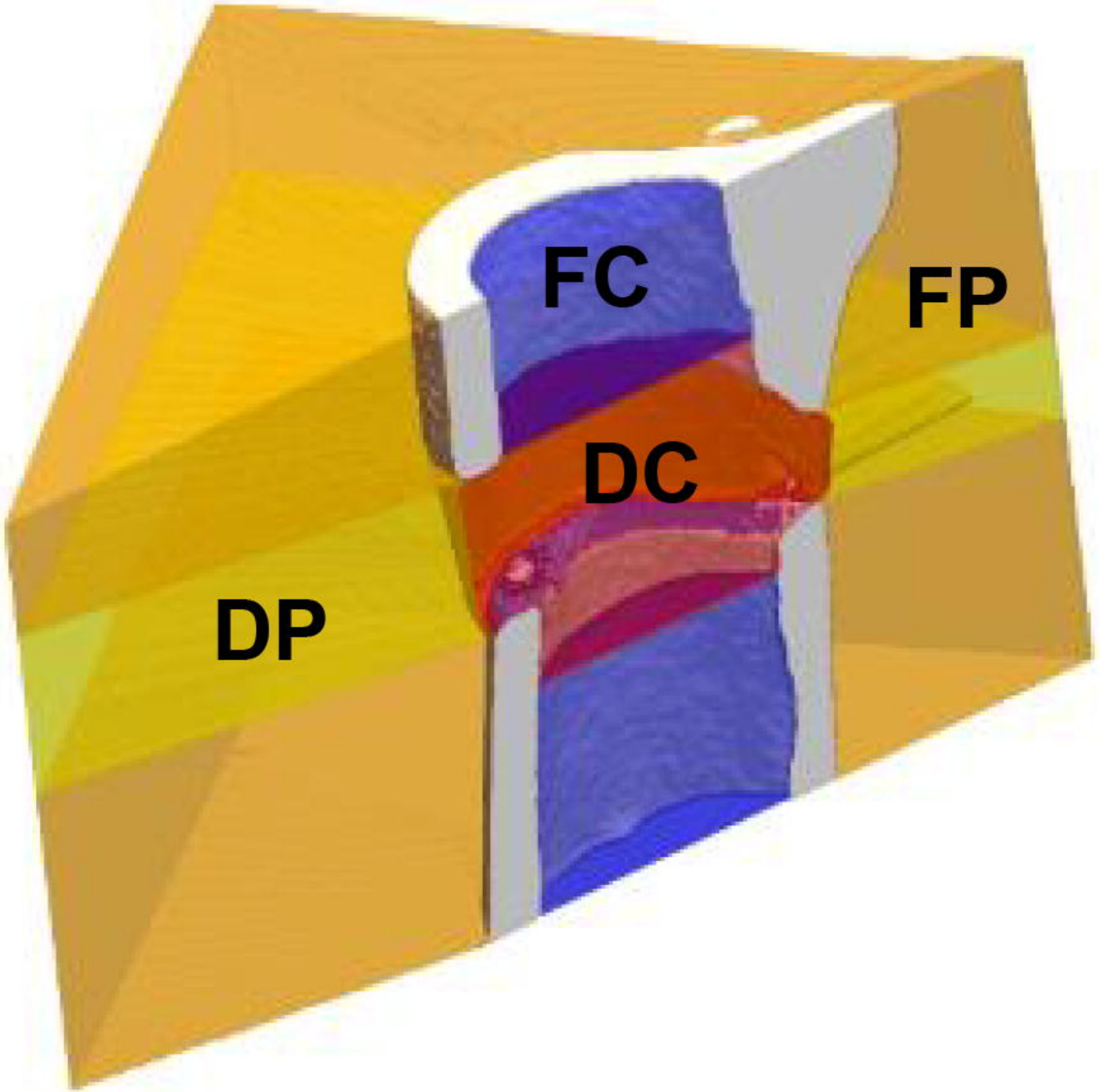

Figure 2

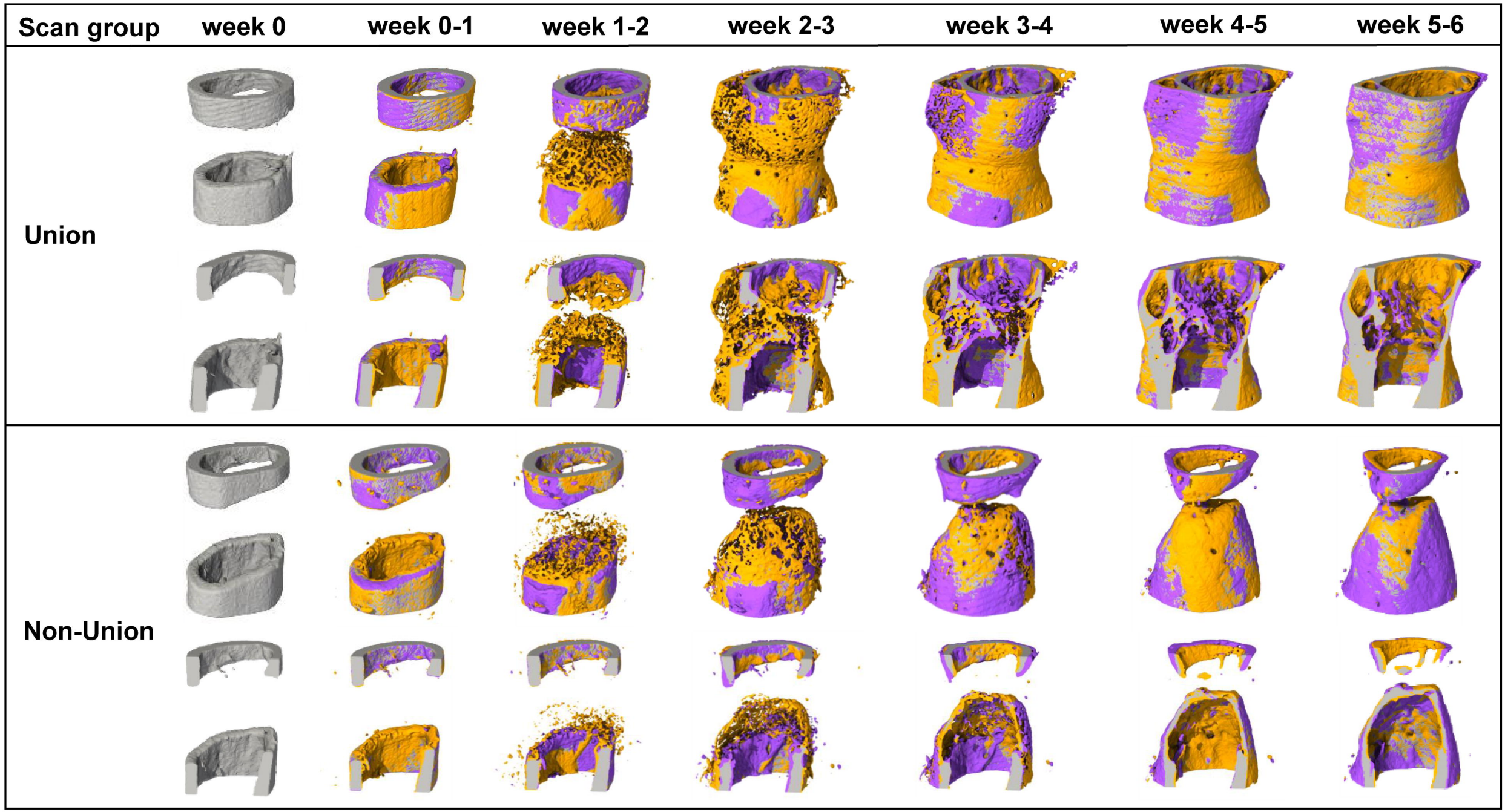
Scan group
week 0
week 0-1
week 1-2
week 2-3
week 3-4
week 4-5
week 5-6
Union
Non-Union

Figure 3

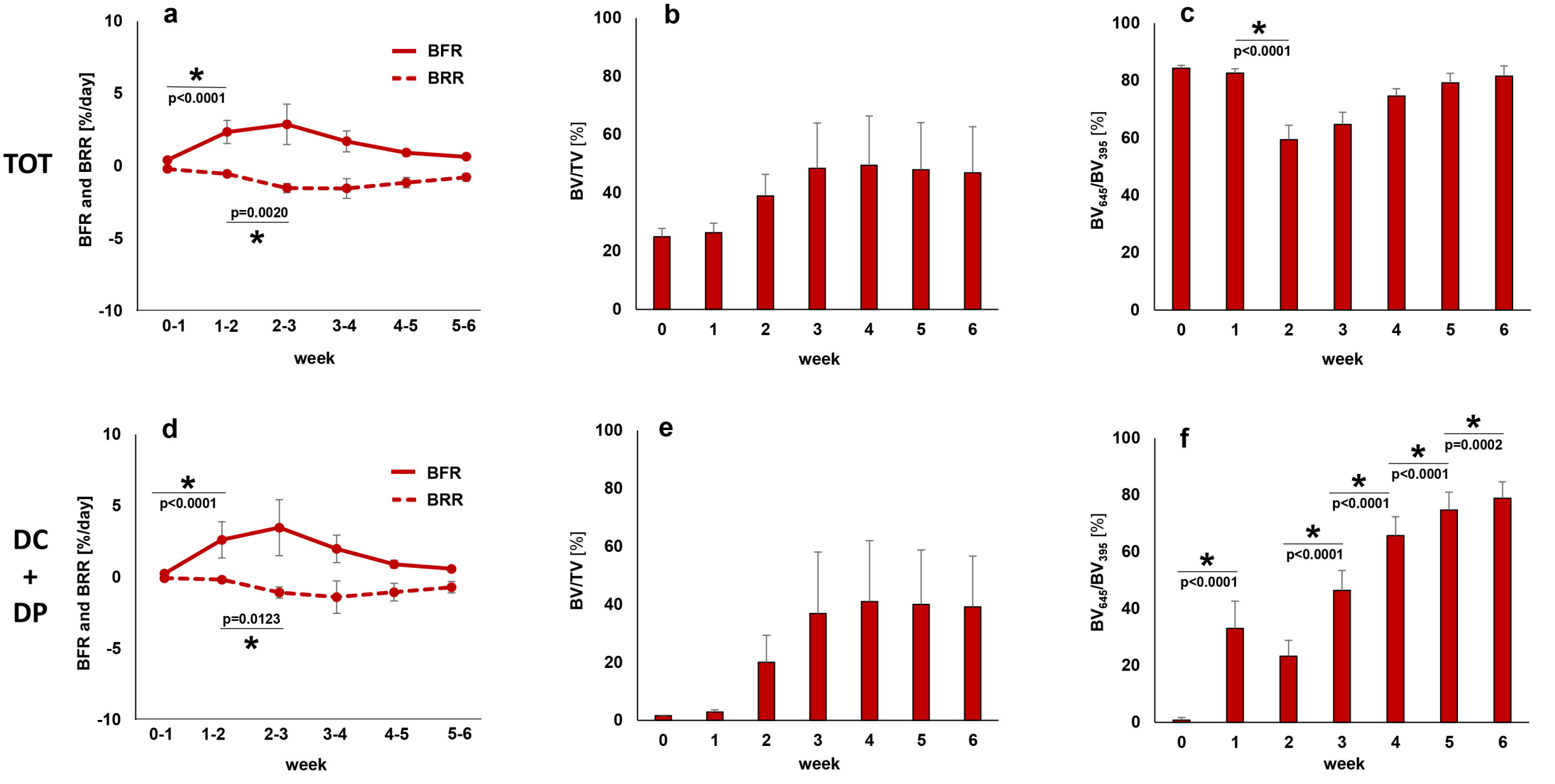
TOT
DC + DP
a
b
c
d
e
f
BFR
BRR
BFR and BRR [%/day]
BV/TV [%]
BV_{645}/BV_{395} [%]
week
0-1
1-2
2-3
3-4
4-5
5-6
p<0.0001
p=0.0020
p=0.0123
p=0.0002

Figure 4

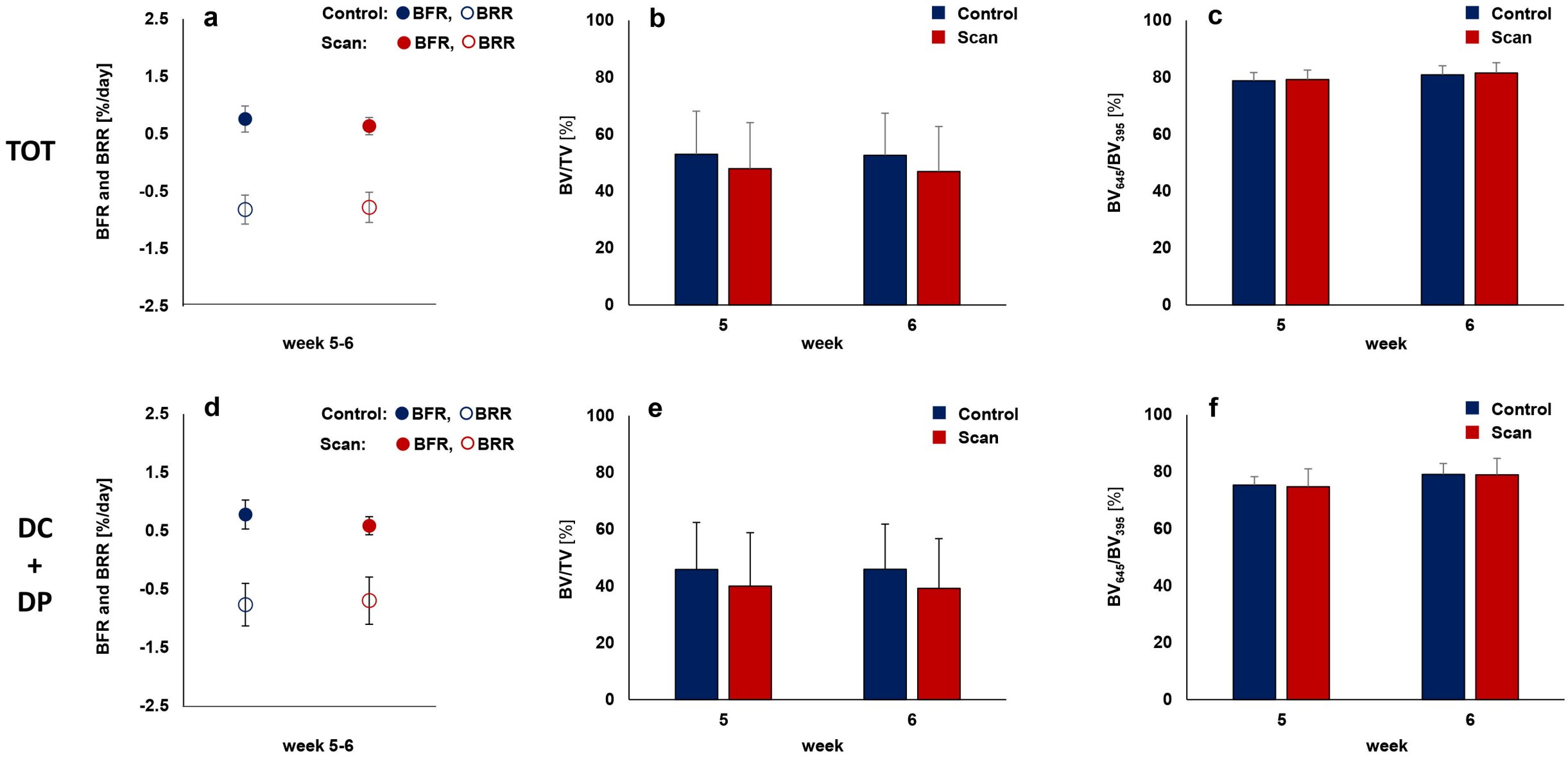
TOT
DC + DP
a
b
c
d
e
f
Control: BFR, BRR
Scan: BFR, BRR
BFR and BRR [%/day]
2.5
1.5
0.5
-0.5
-1.5
-2.5
week 5-6
Control
Scan
BV/TV [%]
100
80
60
40
20
0
5
6
week
BV645/BV395 [%]

Figure 5

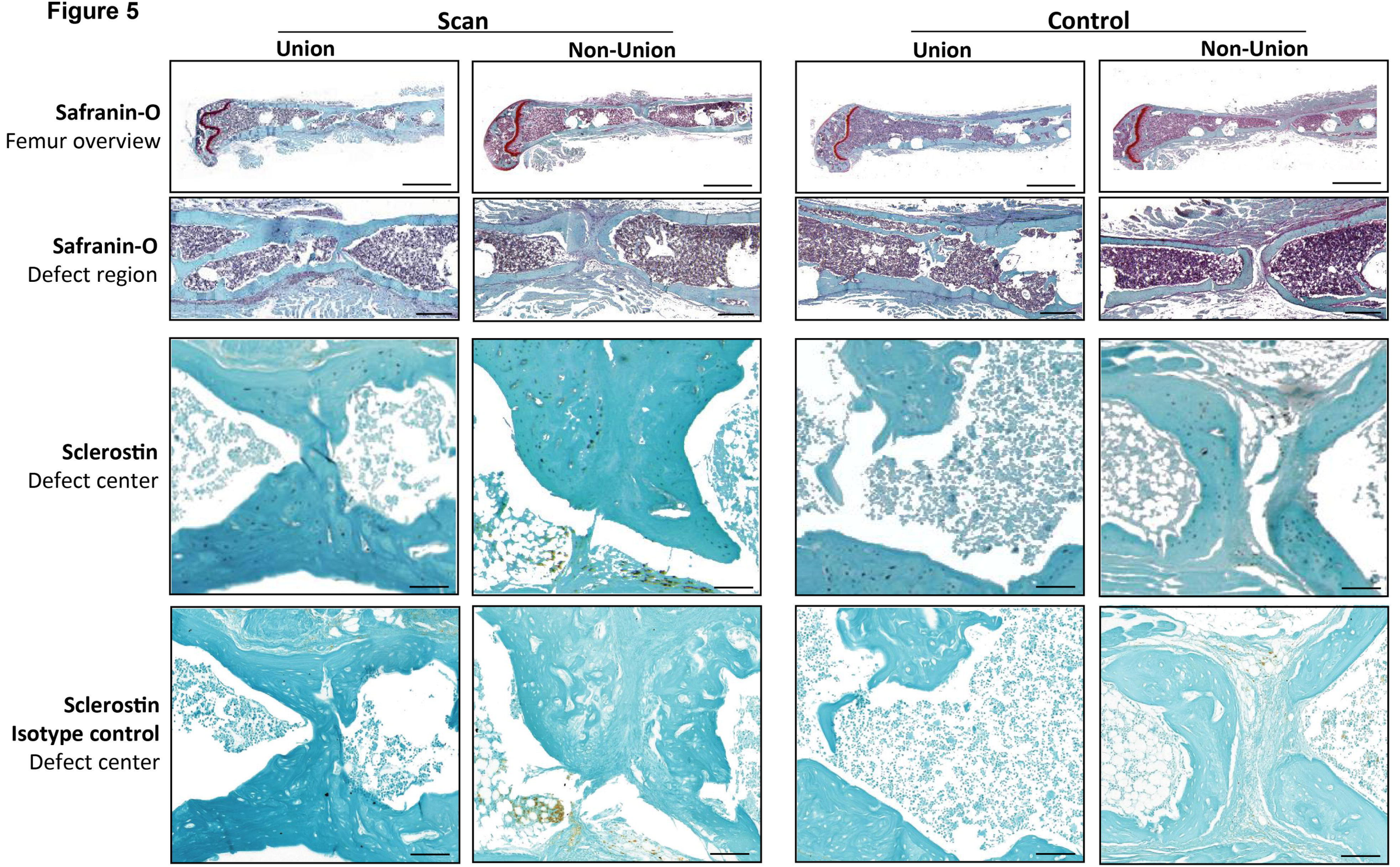
Scan
Control
Union
Non-Union
Union
Non-Union
Safranin-O
Femur overview
Safranin-O
Defect region
Sclerostin
Defect center
Sclerostin
Isotype control
Defect center